Revision 2

1　# Effect of the clay and the metal container in retaining

2　# Sm^{3+} and ZrO^{2+} and the reversibility of the process.

3　SAID EL MRABET[1], MIGUEL A. CASTRO[1], SANTIAGO HURTADO[2], M.

4　MAR ORTA[1], M. CAROLINA PAZOS[3], MARÍA VILLA-ALFAGEME[4], AND

5　MARÍA D. ALBA[1,†]

6

7　[1] Instituto Ciencia de Materiales de Sevilla (CSIC-Universidad de Sevilla).

8　Avda. Américo Vespucio, 49. 41092 Sevilla, Spain.

9　[2] Servicio de Radioisótopo del CITIUS (Universidad de Sevilla).

10　Avda. Reina Mercedes, 4. 41012 Sevilla, Spain.

11　[3] Escuela de Ciencias Químicas, Universidad Pedagógica y

12　Tecnológica de Colombia UPTC.

13　Avda. Central del Norte, Vía Paipa, Tunja, Boyacá, Colombia

14　[4] Dpt. Física Aplicada II (Universidad de Sevilla).

15　Avda. Reina Mercedes, s/n. 41012 Sevilla, Spain.

16

17　**ABSTRACT**

18　Knowledge and understanding about radionuclides retention processes on the materials

19　composing the engineered barrier (clay mineral and metallic container waste) are

20　required to ensure the safety and the long-term performance of radioactive waste

21　disposal. Therefore, the present study focuses on the competitiveness of clay and the

22　metallic container in the process of adsorption/desorption of the radionuclides

23　simulators of Am^{3+} and UO_2^{2+}. For this purpose, a comparative study of the interaction

† *Corresponding author: TEL: +34 954489546*
E-mail: alba@icmse.csic.es

Revision 2

24   of samarium (chosen as chemical analogue for trivalent americium) and zirconyl (as

25   simulator of uranyl and tetravalent actinides) with both FEBEX bentonite and metallic

26   container, under subcritical conditions, was carried out. The results revealed that the

27   AISI-316L steel container, chemical composition detailed on Table 1, immobilized the

28   HRW, even during the corrosion process. The ZrO^{2+} was irreversibly adsorbed on the

29   minireactor surface. In the case of samarium SEM/EDX analysis revealed the formation

30   of an insoluble phase of samarium silicate on the container surface. There was no

31   evidence of samarium diffusion through the metallic container. Samarium remained

32   adsorbed by the container also after desorption experiment with water. Therefore, steel

33   canister is actively involved in the HRW immobilization.

34   **Keyword.** geological disposal, metallic canister, clay minerals, radionuclide

35   waste, actinide, sorption/desorption.

36

37

38

Revision 2

39   **INTRODUCTION**

40

41   The safe disposal of radioactive wastes and specifically the need to protect

42   humans and the environment in the far future is given particular attention in all

43   countries engaged in nuclear power generation. Nowadays, disposal of these wastes in

44   deep geological repositories has been established as the safest and the most

45   environmentally appropriate solution (Alba et al., 2005; Duro et al., 2008; Alba et al.,

46   2009). Repositories are generally designed on the basis of a multiple barrier system

47   which consists mainly of natural and engineered barriers to isolate the hazardous

48   radionuclides from the accessible environment (McCombie et al., 2000; Astudillo,

49   2001; Chapman, 2006). The engineered barrier system (EBS) comprises the respective

50   metallic containers filled with radioactive waste and a backfill clay material, mostly

51   smectite standing between container and host rock in order to avoid the access of

52   groundwater to the high radioactive waste (HRW) as well as its subsequent migration

53   out of repository (Malekifarsani et al., 2009). However, it is impossible to guarantee the

54   long-term stability and integrity of the engineered barrier system. Once the overpack

55   comes into contact with groundwater higher concentrations of CO_3^{2-} ions (Ishidera et

56   al., 2008), it will begin to corrode and, therefore, smectite could interact with dissolved

57   iron, hydrogen gas and other corrosion products of the steel overpack such as magnetite

58   (Fe_3O_4), goethite (FeO(OH)) (Smart et al., 2002; Carlson et al. 2007) or siderite.

59   Therefore, the corrosion of candidate metals for the container as well as the

60   effect of their corrosion products with clay minerals were the subject of many

61   experimental investigations and geochemical modelling (Guillaume et al., 2003;

62   Papillon et al., 2003; Perronnet, 2004; Wilson et al., 2006b; Bildstein et al., 2006).

63   Studies of iron-clay interactions have shown the systematic destabilization of the initial

64   clay mineral and the subsequent crystallization of reaction products (Guillaume et al.,

65   2003, 2004; Lantenois et al., 2005). Lantenois et al. (2003) has investigated the

66   interactions between Fe and a variety of natural and synthetic smectite samples with the

67   aim of determining the effect of crystallo-chemical features on the smectite/iron

68   interactions. At 80°C, the results indicated that oxidation of the container by smectites

69   occurs only for dioctahedral smectites under basic pH conditions, whereas the container

70   corrodes by precipitating magnetite, but without smectite alteration at pHs ranging from

71   slightly acid to neutral. Likewise, Wilson et al. (2006a; 2006b) has investigated the

72   stability of Na-montmorillonite between 80ºC and 250ºC and observed that Fe-rich

73   smectite was formed and they exhibited lower swelling properties than the Na-

74   montmorillonite. Moreover, at 250ºC, berthierine was formed.

75   All these previous studies showed that the effect of container corrosion on the

76   stability of the clay depends on many parameters such as temperature or the nature of

77   the clay minerals. In addition, a geochemical modelling study of iron/clay interactions

78   has been conducted by Samper et al. (2008) and demonstrated that most of the Fe

79   diffuses from the canister into the clay, where it sorbs or precipitates as magnetite.

80   Moreover, as reported in previous study, this magnetite is expected to act as sorbing

81   layer and it is able to delay the diffusion and immobilise many radionuclides under

82   repository conditions (Tiziana Missana et al., 2003). Indeed, several studies have been

83   undertaken to determine the ability of magnetite, commonly formed on corroding steel

84   surfaces, to absorb or reduce some radionuclides (Granizo and Missana, 2006; Rovira

85   et al., 2004). El Amrani et al. (2007) studied sorption of uranium onto magnetite and

86   found that the sorbed uranium is a mixture of tetra- and hexa-valent uranium.

87   In light of these studies, an understanding of the sorption/retention of

88   radionuclides on materials composing the engineered barrier (clay and metallic

Revision 2

89   container waste) is of paramount importance for the long-term performance assessment

90   of nuclear waste repositories. El Mrabet. et al. (2012) have carried out experiments to

91   study the competitive effect of the steel canister and clay barrier on the sorption of Eu^{3+}

92   used as trivalent actinides under reducing conditions and reported that both components

93   of the engineering barrier (clay mineral and metallic canister) were involved in the

94   immobilization of Eu^{3+} by the formation of insoluble europium silicate phases.

95   However, to our knowledge, it is unclear whether this behaviour is general for any

96   actinide in trivalent or other oxidation states. Therefore, the present study focuses on the

97   competitiveness of clay and the steel container in the process of adsorption/desorption

98   of the radionuclide simulators of Am^{3+} and UO_2^{2+}. For this purpose, chemical analogue

99   simulators were chosen; Sm^{3+} as simulator of trivalent Am and zirconyl as simulator of

100   uranyl and tetravalent actinides. The FEBEX bentonite was selected as simulator of the

101   materials of the engineered barrier and the austenitic stainless steel AISI-316L as

102   simulator of the metallic material.

103

104   **EXPERIMENTAL METHODS**

105

106   **Experimental design and materials.**

107

108   The clay mineral used in this study (Bentonite FEBEX) has been extensively

109   investigated as a suitable component of the engineered barrier in the recent past in many

110   countries in Europe and around the world (Triphaty et al., 2004). This bentonite was

111   provided by the ENRESA Company (the Spanish Company in charge of radioactive

112   wastes   management)   and   has   the   structural   formula:

113   $(Ca_{0.5}Na_{0.08}K_{0.11})(Si_{7.78}Al_{0.22})(Al_{2.78}Fe^{3+}_{0.33}Fe^{2+}_{0.02}Mg_{0.81})O_{20}(OH)_4$. Its main phase is

Revision 2

114   montmorillonite (smectite percentage higher than 90%) together with small amounts of

115   quartz (Fernandez et al., 2004).

116        $Sm(NO_3)_3 \cdot 6H_2O$ and $ZrO(NO_3)_2 \cdot 7H_2O$ which are commercially available from

117   Sigma-Aldrich, were used in this work as possible chemical analogues for long-lived

118   actinides present in HRW, Sm as simulator of trivalent Am and zirconyl as simulator of

119   uranyl and tetravalent actinides (Chapman and Smellie, 1986).

120   Copper, titanium, stainless steels, were chosen in a number of disposal concepts

121   as suitable materials for the canisters. Also, they exhibit a high attack resistance in the

122   expected disposal environment (Rebak, 2006). Therefore, in the present study,

123   hydrothermal experiments were carried out in a stainless steel AISI-316 L reactor,

124   (selected as candidate container), commercially available, the chemical composition is

125   given in Table 1.

126   A deep understanding of the competitive effect of the canister material in the

127   processes by which the bentonite retains radioactive waste is of great importance for the

128   long term stability of the engineered barrier system. For this purpose, a minireactor

129   made from the same material as the steel reactor was designed by us. Thus, 300 mg of

130   the powdered bentonite was placed into a cylindrical steel cell (minireactor). The

131   bentonite-minireactor set was then compacted in a cylindrical die, (experimental design

132   has been described in detail by El Mrabet et al., 2012). Finally, the compacted set was

133   placed into the steel reactor and submitted to a hydrothermal treatment. The

134   hydrothermal reactions were carried out with 7.9×10^{-2} M of each solution of Sm^{3+} or

135   ZrO^{2+} at 300ºC for 4.5 days.

136   Despite of the expected temperature in the disposal repositories will not exceed

137   150ºC, many studies have been carried out by simulating the deep geological disposal at

138   temperatures up to 350ºC to increase the reaction rate (Mathers et al., 1982; Savage and

Revision 2

139   Chapman, 1982; Allen et al., 1988, Alba and Chain., 2007). Therefore, in the present

140   study, higher temperatures were taken account as necessary conditions to increase the

141   reaction rate and run the experiments at laboratory scale.

142   Desorption study was carried out by washing both treated minireactors with

143   distilled water until the washed water reached a neutral pH.

144

145   **Characterization methods.**

146

147   The X-ray diffraction patterns were obtained using an X'Pert Pro

148   PANALYTICAL diffractometer in the conventional $\theta - 2\theta$ Bragg–Brentano

149   configuration using Cu Kα radiation. Diffragtograms were registered from 3º to 70º 2θ

150   and in steps of 0.05º in random powder mode.

151   The morphology and chemical composition of both the steel and clay mineral

152   before and after hydrothermal treatment with the Sm^{3+} or ZrO^{2+} solution at 300ºC for

153   4.5 days were investigated using a SEM-FEG HITACHI S- 4800 a scanning electron

154   microscope equipped with an Xflash 4010 (BRUKER) for energy dispersive X-ray

155   (EDX) analysis. The EDX spectra were taken in point analysis mode.

156   In order to obtain useful information about the oxide scale structure, a detailed

157   cross-sectional study involving SEM observations in combination with EDX line profile

158   along a representative area of the minireactor was performed.

159   The pH and Eh of the supernatant were measured at room temperature using a

160   Eutech Instruments PC 700 pH-meter before and after the hydrothermal treatment in

161   aerobic conditions.

162

163

Revision 2

164   **RESULTS**

165

166   **Sorption of Sm^{3+} on the FEBEX smectite**

167

168   The XRD pattern of untreated clay mineral (Fig. 1a) exhibited typical reflections

169   of montmorillonite with a series of narrow and sharp peaks indicating its crystalline

170   structure. The basal spacing d_{001} which corresponds to a value of about 1.4 nm is

171   associated to the bilayer hydrated Ca^{2+} in the smectite clay interlayer (Chain, 2007).

172   Additionally, the XRD showed narrow peaks that correspond to quartz (PDF 04-006-

173   1757) and cristobalite (PDF 04-008-7824). After hydrothermal treatment with Sm^{3+}

174   (Fig. 1b), the montmorillonite remains as the main constituent of the clay mineral and

175   the quartz is now absent but new impurities, $H_2Si_2O_5$ (PDF 00-050-0439) and Nacrite-

176   2M2 (PDF 01072-2206), are observed. The strongest peak that appears at 2θ value of

177   6.33º, which corresponds to [001] lattice plane, shifted after hydrothermal treatment to a

178   lower diffraction angle 5.84º, thus implying an increase in basal spacing d_{001} which may

179   be attributed to the sorption of hydrated M^{3+} cations into the interlayer space (Alba et

180   al., 2001). Previous studies demonstrated that the hydrothermal treatment of clay

181   minerals in the presence of the canister does not provoke a decreasing of its swelling

182   capacity, (Bildstein et al, 2006; Carlson et al., 2007; Gaudin et al., 2009; Savage et al.,

183   2010). The 060 reflection of FEBEX does not change after hydrothermal treatment and

184   was found to be 0.149 nm as expected for dioctahedral smectites (Davitz and Low,

185   1970).

186   The SEM micrographs of FEBEX before and after hydrothermal treatment with

187   Sm^{3+} at 300ºC for 4.5 days are shown in (Fig.2). The untreated clay showed the lamellar

188   morphology for the most particles (Fig. 2a). Furthermore, the typical $K_{\alpha 1}$ lines for Si,

Revision 2

189   Mg, Al and Ca in montmorillonite can be seen in the corresponding EDX spectrum,

190   (Fig. 2d). In the case of the reacted clay mineral with Sm^{3+}, the most particles exhibited

191   a lamellar morphology as can be seen in Fig. 2b, the associated EDX spectrum (Fig. 2e)

192   showed the typical $K_{\alpha 1}$ lines for Si, Mg and Al of FEBEX, $L_{\alpha 1}$ and $L_{\beta 1}$ lines of Sm

193   which indicated that Sm was absorbed in the interlayer space of the FEBEX bentonite.

194   The decrease of the Mg content and the absence of Ca when compared to the original

195   FEBEX are due to the leaching of Mg^{2+} ions and the exchange of Ca^{2+} by Sm^{3+} in the

196   interlayer space, which is in accordance with the observed lamellar expansion by XRD.

197   Besides those lamellar particles, some compact block particles (Fig. 2c, ①) were also

198   observed with chemical composition associated to the phases containing samarium

199   which were not detected by XRD (Figs. 2f). It should be noted that the presence of

200   chromium is due to the degradation of the minireactor (see the chemical composition of

201   the steel reactor in Table 1).

202

203   **Sorption of Sm^{3+} on the minireactor.**

204

205   The XRD patterns of the minireactor after hydrothermal treatment at 300°C for

206   4.5 days in contact with a solution of Sm^{3+} 7.9×10^{-2} M (Fig. 3a) showed that the original

207   austenitic metallic matrix of the steel (see it chemical composition in Table 1) remains

208   as the dominating phase. Additionally, a considerable portion of phases containing iron

209   (goethite) from container degradation marked by ② as well as other phases containing

210   samarium marked by①, ③ and ④ were also observed. Under scanning electron

211   microscopy, the surface of the reactor appears to be entirely covered by a thin layer of

212   oxide (Fig. 4a). The EDX spectrum showed the spectral lines of the austenitic phase

213   together with Sm peaks (Fig. 4g).

Revision 2

214   After hydrothermal reaction with FEBEX and Sm^{3+} solution, (Fig. 3b), the

215   dominant peaks in the X-ray diffraction pattern of the minireactor corresponds to the

216   original austenitic phase. Furthermore, minor phases such as samarium aluminate

217   ($SmAlO_3$, PDF 00-22-1307), samarium oxide (Sm_2O_3, PDF 01-076-0153) and

218   clinozoisite ($Ca_2Al_3(SiO4)(Si_2O_7)O(OH)$, PDF 00-44-1400) which contains elements

219   leached from the clay mineral were also detected. As can be seen by SEM micrographs,

220   Fig. 4b, a homogeneous compact thin layer formed by small crystals covers the entire

221   surface of the reactor. According to the EDX analysis, the higher Sm/Si ratio together

222   with weak intensity of K_α lines of Al and Mg arising from clay minerals particles

223   implies that the thin layer of oxide was Si- and Sm- rich, (Fig. 4h). The thickness of

224   this layer is corroborated by the maintenance of Cr/Fe intensity ratio in the EDX

225   spectra, (Figs. 4f-4h). Beside this, some compact block particles (Fig. 4c, ①) with a

226   chemical composition associated with samarium silicate were also observed (Figs. 4i).

227   In order to get a deeper insight about the diffusion of samarium into the

228   minireactor and the distribution of the chemical elements in the oxide layer formed after

229   hydrothermal reaction, a cross-sectional study involving SEM observations combined

230   with EDX line profile along a representative area (white line in Fig. 5a) of the

231   minireactor was performed. This study showed that the oxide scale is thin and mainly

232   composed of samarium silicate at the scale-atmosphere interface (Fig. 5b). There was no

233   evidence of samarium diffusion towards the metallic container, which is in accordance

234   with the results obtained by surface EDX analysis.

235

236   **Desorption of Sm^{3+} on the minireactor.**

237

238   When the steel was submitted to desorption process after hydrothermal

239   treatment, the identified species by XRD pattern (Fig. 3c) are the same as those seen

240   previously in the reactor post-treatment. Nevertheless, the top surface morphology of

241   the oxide scale formed over the steel changes significantly when comparing to that of

242   the reactor post-treatment. SEM micrographs showed that the minireactor surface is

243   covered by a fine-grain oxide layer intercalated in some areas by a very thin layer of

244   samarium silicate (Figs. 4d-4j). Besides this, agglomerations of small particles (Fig. 4e,

245   ②) were also observed with a chemical composition compatible with samarium silicate

246   as stated by EDX spectrum (Figs. 4k). However, as can be seen in Figs. 5c-5d, the cross

247   sectional study of the reactor hardly revealed the presence of samarium silicate whose

248   thickness has been significantly reduced with respect to the reactor post-treatment.

249

250   **Sorption of ZrO^{2+} on the FEBEX smectite**

251

252   The XRD patterns of the reacted clay FEBEX with a solution of ZrO^{2+} 7.9×10^{-2}

253   M at 300ºC for 4.5 days, (Fig. 6b) showed that the basal spacing d_{001} expanded from

254   1.40 nm to 1.46 nm, suggesting that the interlayer cation exchange between the initial

255   (Ca^{2+} and Na^+) by ZrO^{2+} has been occurred. Also, the persistence of the d- spacing of

256   1.49 nm peak without any reflection to a higher 2θ angle indicated no leaching of the

257   octahedral cations. It can also be noticed form XRD analysis that neither phases

258   resulting from minireactor degradation, nor those containing zirconium were detected in

259   the treated clay minerals, which is probably due to their small crystalline size. SEM

260   micrographs of the reacted FEBEX with ZrO^{2+} showed the typical lamellar morphology

261   for the most of particles with a chemical composition compatible with ZrO^{2+}as

262   interlayer cations, (Figs. 7a-7d). In addition to these lamellar particles and under

263   backscattering electron beam, agglomerations of small particles with brilliant

264   appearance (Fig. 7b, ①) were also observed with a chemical composition consisting

265   mainly of phase containing zirconium, (Figs. 7e). Moreover, the SEM/EDX analysis of

266   other zone (labelled ② in Fig. 7c) indicated that the treated clay mineral was

267   significantly enriched in iron, which suggested the release of the iron upon degradation

268   of the container, (Figs. 7f).

269   Finally, it is remarkable that the corresponding EDX spectra were characterised

270   by the $K_{\alpha 1}$ lines of Si, Al, Mg and L_α line of Zr. Thus, there was no evidence of the

271   existence of isolated zirconium silicate, the zirconium being associated to the clay

272   mineral phase. Similar observations were seen in the case of the treated clay with Sm^{3+}.

273

274   Sorption of ZrO^{2+} on the minireactor

275

276   The XRD patterns of the minireactor treated hydrothermally at 300ºC for 4.5

277   days in contact with a solution of ZrO^{2+} 7.9×10^{-2} M (Fig. 8a) showed the austenite as the

278   dominating metallic phase of the steel which suggested that the minireactor did not

279   undergo any noticeable change in term of phase transformation due to the hydrothermal

280   treatment. Additionally, a considerable portion of iron oxide, hematite (Fe_2O_3, PDF 01-

281   085-0987), as well as minor phases of zirconium oxide, baddeleyite (ZrO_2, PDF 00-013-

282   0307), were detected. The SEM micrographs of the minireactor revealed that the surface

283   is entirely covered by a thin layer of crystals of various size mainly composed of

284   zirconium oxide as shown in Figs. 9a-9g.

285   After reaction with clay minerals and ZrO^{2+} at 300ºC for 4.5 days, no changes

286   were observed with respect to the previous sample in the XRD pattern (Fig. 8b); the

287   dominant species remain the austenitic metallic matrix of the steel and iron oxide

Revision 2

288   (Fe_2O_3). In the latter, the diffraction lines are less intense than those observed in the

289   treated reactor without FEBEX. The baddeleyite signals remain also poorly intense. As

290   can be seen from the SEM micrographs (Fig. 9b), the steel surface is covered by a thin

291   layer of fine-grain oxide composed mainly of zirconium oxide as observed in the EDX

292   spectrum, (Fig. 9h). Furthermore, the $K_{\alpha 1}$ lines for Si, Mg and Al arising from clay

293   minerals particles are visible in the associated EDX spectrum. Besides this, some

294   isolated agglomerates together with bright dispersed areas (labelled ① and ②

295   respectively in Figs. 9c-9d) appear over the steel surface (Figs. 9c-9d). According to

296   EDX analysis, the agglomerates were Zr-rich (Fig. 9i), whereas the bright areas were

297   clay minerals rich particles with some zirconium (Fig. 9j) compatible with the ZrO-

298   FEBEX observed by XRD. The SEM cross-sectional analysis (white line in Fig. 10a)

299   only showed the presence of zirconium oxide at the scale-atmosphere interface without

300   its diffusion towards the container which is in agreement with results obtained by EDX

301   surface analysis (Fig. 10b).

302

303   **Desorption of ZrO^{2+} from the minireactor.**

304   Fig. 8c shows the XRD diffraction pattern of the reactor after the desorption

305   process. The dominant phase was the austenitic pattern arising from the metallic matrix

306   of the steel remains. In addition, some iron oxides and zirconium oxides were detected.

307   These results were similar to those of the post-treatmented reactor which suggests that

308   the reactor did not undergo any structural change.

309   The morphology of the oxide layer is also similar to that of the reactor after the

310   treatment; the scale is formed by fine–grain oxide crystals over which a few hexagonal

311   crystals are growing, (Figs. 9e-9f). According to EDX analysis (Figs. 9k-9l), the

312   hexagonal crystals (labelled as ④) are of similar composition to that of the small

Revision 2

313   crystals (labelled as ③) but with higher zirconium content. Furthermore the the $K_{\alpha 1}$

314   lines for Si, Al and $L_{\alpha 1}$ were detected in the corresponding EDX spectrum which

315   indicated the formation of an insoluble zirconium silico-aluminate. Unfortunately, no

316   phases containing zirconium were identified by cross sectional study because the layer

317   is too thin to be analysed in cross section, therefore no information was provided as can

318   be seen in (Figs. 10c-10d).

319

320   **Supernatant characterization**

321

322   The electrochemical properties of the initial solution and supernatant are shown

323   in Table 2. The results showed that the initial pH value decreased from 4.2 to about 2.5

324   for Sm^{3+}, whereas for ZrO^{2+}, the post-quench pH values before and after hydrothermal

325   treatment remained quasi-alike. In both cases, the pH values indicated an acidic medium

326   of the supernatant solutions. No structural transformation at those acidic conditions was

327   observed in the XRD patterns for the both treated clay minerals (e.g. swelling capacity).

328   That agrees with Lantenois et al. (2005) which observed that the destabilization of

329   smectite in contact with metallic Fe at a pH lower than 7 is not significant. The

330   Pourbaix diagram showed that the E_h and pH values measured for both solutions favour

331   samarium and zirconium as Sm^{3+} and ZrO^{2+} ions respectively in water as ideal solution.

332

333   **DISCUSSION**

334

335   As discussed above by XRD and SEM analysis, the interaction between

336   zirconium and FEBEX involved only sorption at the cation-exchange sites located in the

337   interlayer spaces of the clay. Additionally, no evidence of phases appearing as a result

Revision 2

338   of the chemical interactions of radioactive waste with clay minerals barrier such as

339   zirconium silicates was observed. The generation of these phases is especially important

340   when the suitable properties of the engineered barrier (clay minerals barrier) such as

341   swelling capacity and cation exchange failed to retain the radionuclide. Furthermore, the

342   released iron particles upon container degradation detected by EDX analysis did not

343   provoke a decrease of the swelling properties of the clay mineral. The interaction of

344   ZrO^{2+} with the minireactor was only superficial and no zirconium diffusion towards the

345   metallic container was detected. Moreover, the adsorbed zirconium was retained, even

346   after desorption process (hexagonal crystals) which implies the irreversible participation

347   of the metallic container in the sorption of zirconyl taken as stable uranyl simulator.

348   These findings regarding the active participation of the container in the sorption of

349   ZrO^{2+} under subcritical conditions are in agreement with previous study by Gimenez et

350   al. (2007) who studied the sorption of As(III) and As(V) on different natural iron oxides

351   (hematite, magnetite, and goethite) and found that the hematite showed higher sorption

352   capacity, especially at acidic pH. Additionally, these iron oxide phases have also a

353   relevant role on the retention of radionuclides such as U and Np from the repository and

354   the surrounding rocks, as predicted by Meijer (1990).

355   Nevertheless, in the case of Sm^{3+}, besides the cation-exchange at the interlayer

356   spaces of the clay, the samarium had also precipitated out of solution to form a solid

357   phase by leaching of cations, mainly sodium or calcium released by ion exchange

358   process. Despite the XRD diffraction pattern did not show any samarium silicate phase

359   provided by the mixed solution of the clay mineral, Sm^{3+} and container; SEM/EDX

360   analysis indicated the generation of an insoluble disilicate phase with a chemical

361   composition compatible with samarium silicate on both the clay minerals and the steel

362   container. Furthermore, the interaction of Sm^{3+} with the minireactor was on the surface

Revision 2

363   and has not been diffused into the metallic container. This samarium silicate layer

364   remained, but very thin, after desorption process. These findings regarding to the active

365   participation of both components of the engineered barrier in the sorption of Sm^{3+} under

366   subcritical conditions are in contrast to those of Parfitt et al. (1980) who reported that

367   the presence free iron oxides inhibits the sorption by the whole soil. This inhibition was

368   explained by the Fe coating of clay mineral in red earth which suppresses Eu^{3+} sorption.

369   Also, as reported by Wang et al. (2000), these iron oxides in red earth are not a

370   significant sink for Eu^{3+}.

371   Finally, it is also mentioned that the behaviour of Sm^{3+} is similar to that of Eu^{3+}

372   (El Mrabet et al. 2012). In the case of Eu^{3+}, the amount of europium silicate retained by

373   the container remained even after the desorption process with a thickness of ca. 5 μm,

374   whereas in the case of Sm^{3+}, the samarium silicate layer was too thin to be detected by

375   EDX line profile.

376

377   **CONCLUSIONS**

378

379   The main conclusions that can be drawn from the above results are:

380   ✓ The interaction between FEBEX and Sm^{3+} involved both sorption at the

381   cation exchange sites located in the interlayer spaces of the clay mineral

382   and the chemical interaction with the generation of an insoluble phase of

383   samarium silicate. In the case of ZrO^{2+}, this interaction revealed only

384   sorption of hydrated cations into the interlayer space.

385   ✓ From both studies with Sm^{3+} and ZrO^{2+}, we can deduce that the metallic

386   canister is actively involved in the immobilization of HRW, even during

387   the corrosion process.

Revision 2

388

ACKNOWLEDGMENTS

390

393

REFERENCES CITED

395

396   Alba, M.D., Becerro, A.I., Castro, M.A., and Perdigón, A.C. (2001). Hydrothermal

397   reactivity of Lu-saturated smectites: Part I. A long-range order study. American

398   Mineralogist, 86, 115-123.

399   Alba, M.D., and Chain, P. (2005). Interaction between lutetium cations and 2:1

400   aluminosilicates under hydrothermal treatment. Clays and Clay Minerals, 53,

401   39–46.

402   Alba, MD., and Chain, P. (2007). Persistence of lutetium disilicate. Applied

403   Geochemistry, 22, 192-201.

404   Alba, M.D., and Chain, P. (2009). Chemical reactivity of argillaceous material in

405   engineered barrier: Rare earth disilicate formation under subcritical conditions.

406   Applied Clay Science, 43, 369–375.

407   Allen, C.C, and Wood M.I. (1988). Bentonite in nuclear waste disposal: A review of

408   research in support of the Basalt Waste Isolation Project. Appled Clay Science,

409   3, 11-30.

410   Astudillo, J. (2001). El almacenamiento geológico profundo de los residuos radiactivos

411   de alta actividad. Principios básicos y tecnología. ENRESA, Madrid.

412   Bildstein, O., Trotignon, L., Perronnet, M., and Jullien, M. (2006). Modelling iron-clay

413   interactions in deep geological disposal conditions. Physics and Chemistry of

414   the Earth, 31, 618-625.

415   Carlson, L., Karnland, O., Oversby, V.M., Rance, A.P., Smart, N.R., Snellma, M.,

416   Vähänen, M., and Werme L.O. (2007). Experimental studies of the interactions

417   between anaerobically corroding iron and bentonite. Physics and Chemistry of

418   the Earth, 32, 334-345.

419   Chain, P. (2007). Estudio del sistema saponita/Lu(NO$_3$)$_3$/H$_2$O en condiciones

420   hidrotermales. Ph.D Thesis Doctoral. University of Seville (Spain).

421   Chapman, N. (2006). Geological disposal of radioactive waste – concept, status and

422   trends. Journal Iberoamerican Geology, 32, 7-14.

423   Chapman, A.N., and Smellie J.A.T. (1986). Introduction and summary of the workshop,

424   Chemical Geology, 55, 167-173.

425   Corma, A., Mifsud, A., and Sanz, E. (1987). Influence of the chemical-composition and

426   textural characteristics of Palygorskite on the acid leaching of octahedral cations.

427   Clay Minerals, 22, 225–232.

428   Davidtz, J.C., and Low, P.F. (1970). Relation between crystal-lattice configuration and

429   swelling of montmorillonites. Clays and Clay Minerals, 18, 325–332.

430   Duro, L., El Aamrani, S., Rovira, M., Pablo, J., and Bruno, J. (2008). Study of the

431   interaction between U(VI) and the anoxic corrosion products of carbon steel.

432   Applied Geochemistry, 23, 1094-1100

433   El Aamrani, S., Gimenez, J., Rovira, M., Seco, F., Grive, M., Bruno, L., Duro, L., and

434   de Pablo J. (2007). A spectroscopic Study of uranium (VI) interaction with

435   magnetite. Applied Surface Science, 253, 8794-8797.

Revision 2

436   El Mrabet, S., Astudillo, J., Castro, M.A., Hurtado, S., Orta, M.M., Pazos, M.C., Rueda,

437   S., Villa, M., and Alba M.D. (2012) Competitive effect of the metallic canister

438   and clay barrier on the sorption of Eu^{3+} under subcritical conditions, 5th

439   International Meeting on Clay in Natural & Enginerred Barriers for Radioactive

440   Waste Confinement, Montpellier (France).

441   Fernandez, A., Baeyens, B., Bradbury, M., and Rivas, P. (2004). Analysis of the

442   porewater chemical composition of a Spanish compacted bentonite used in an

443   engineered barrier. Physics and Chemistry of the Earth., 29, 105-118.

444   Gaudin, A., Gaboreau, S., Tinseau, E., Bartier, D., Petit, S., Grauby, O., Foct, F., and

445   Beaufort, D. (2009). Mineralogical reactions in the Tournemire argillite after in-

446   situ interaction with steels. Applied Clay Science, 43, 196-207.

447   Gimenez, J., Martínez, M., de Pablo, J., Rovira, M., and Duro L. (2007). Arsenic

448   sorption onto natural hematite, magnetite, and goethite. Journal of the Hazardous

449   Materials 141, 575–580.

450   Granizo, N., and Missana, T. (2006). Mechanisms of cesium sorption onto magnetite.

451   Radiochimica Acta, 94, 671–677.

452   Grim, R.E. (1968). Clay Mineralogy. McGraw-Hill Book Company, New York.

453   Guillaume, D., Neaman, A., Cathelineau, M., Mosser-Ruck, R., Peiffert, C.,

454   Abdelmoula, M., Dubessy, J., Villiéras, F., Baronnet, A., and Michau, N. (2003).

455   Experimental synthesis of chlorite from smectite at 300 ºC in the presence of

456   metallic Fe. Clay Minerals, 38, 281–302.

457   Guillaume, D., Neaman, A., Cathelineau, M., Mosser-Ruck, R., Peiffert, C.,

458   Abdelmoula, M., Dubessy, J., Villiéras, F., and Michau N. (2004). Experimental

459   study of the transformation of smectite at 80 and 300 ºC in the presence of Fe

460   oxides. Clay Minerals, 39, 17–34.

Revision 2

461   Ishidera, T., Ueno, K., Kurosawa, S., and Suyama, T. (2008). Investigation of

462   montmorillonite alteration and form of iron corrosion products in compacted

463   bentonite in contact with carbon steel for ten years. Physics and Chemistry of the

464   Earth 33, S269-S275

465   Komadel, P., Madejová , J., Janek, M., Gates, W.P., Kirkpatrick, R.J., and Stucki, J.W.

466   (1996). Dissolution of hectorite in inorganic acids. Clays and Clay Minerals, 44,

467   228–236.

468   Lantenois, S. (2003). Réactivité fer métal/smectites en milieu hydraté à 80°C. PhD

469   thesis, Université d'Orléans, Orléans, France, pp 188.

470   Lantenois, S., Lanson, B., Muller, F., Bauer, A., Jullien, M., and Plançon, A. (2005).

471   Experimental study of smectite interaction with metal Fe at low temperature: 1.

472   Smectite destabilization. Clays and Clay Minerals, 53, 597-612.

473   Malekifarsani, A, and Skachik, M.A., (2009). Calculation of maximum release rates in

474   alternative design changes in the thickness of the buffer for the engineered

475   barrier system (EBS) in deep repository by using Amber code, 51, 355-360.

476   Mather,   J.D.,   Chapman,   N.A.,   Black,   J.H.,   and   Lintern,   B.C.   (1982).

477   The geological disposal of high-level radioactive waste- a review of the Institute

478   of geological sciences research-program. Nuclear Energy-Journal of the British

479   Nuclear Energy Society, 21, 167-173

480   McCombie, C., Pentz, D.L., Kurzeme, M., and Miller, I. (2000). Deep geological

481   repositories: a safe and secure solution to disposal of nuclear wastes. In

482   GeoEng2000 – An international conference on geotechnical & geological

483   engineering,   19-24   November   2000.   Melbourne,   Australia.   Lancaster,

484   Technomic.

Revision 2

485   Meijer, A. (1990). A strategy for the derivation and use of sorption coefficients in

486   performance assessmenct alculations for the Yucca Mountain site. Pg. 9-40.

487   Proceeding of the DOE/yucca Mountain Site Characterization Project

488   Radionuclide Adsorption Workshop at Los Alamos Laboratory. LA

489   12325~C(NNA.19930629.0011).

490   Missana, T., Garcia-Gutierrez, M., and Fernandez, V. (2003). Uranium (VI) sorption on

491   colloidal magnetite under anoxic environment: experimental study and surface

492   complexation modelling. Geochimica et Cosmochimica Acta, 67, 2543-2550.

493   Papillon, F., Jullien, M., and Bataillon C. (2003). Carbon steel behaviour in compacted

494   clay: two long term tests for corrosion prediction. In: Féron, D., MacDonald,

495   D.D. (Eds.), Prediction of the long term corrosion behaviour in nuclearwaste

496   systems. European Federation of Corrosion Publications, vol. 36. Maney

497   Publishing, UK, pp. 439–454.

498   Parfitt, R.L. (1980). Chemical properties of variable charge soils In: Theng, B.K.G.

499   (ed.). Soils with Variable Charge. New Zealand Soc. Soil Sci., Bureau, Lower

500   Hutt, pp. 167–194.

501   Perronnet, M. (2004). Réactivité des matériaux argileux dans un contexte de corrosion

502   métallique. Application au stockage des déchets radioactifs en site argileux. PhD

503   Thesis, Institut National Polytechnique de Lorraine, Nancy, France, p 283.

504   Rebak, R.B. (2006). Selection of Corrosion Resistant Materials for Nuclear Waste

505   Repositories. Report of Lawrence Livermore National Laboratory, UCRL-

506   PROC-221893

507   Rovira, M., de Pablo, J., Casas, I., Giménez, J., and Clarens, F. (2004). Sorption of

508   caesium on commercial magnetite with low silica content: experimental and

509   modelling. Materials Research Symposium Proceedings, 807, 677–682.

Revision 2

510   Samper, J., Chuanhe, L., and Montenegro, L. (2008). Reactive transport model of

511   interactions of corrosion products and bentonite. Physics and Chemistry of the

512   Earth, 33, S306–S316.

513   Savage, D., and Chapman, N.A. (1982). Hydrothermal behaviour of simulated waste

514   glass- and waste-rock ineraction under repository conditions. Chemical Geology,

515   36, 59-86.

516   Savage, D., Watson, C., Benbow, S., and Wilson, J., (2010). Modelling iron-bentonite

517   interaction. Applied Clay Science, 47, 91-98.

518   Smart, N.R., Blackwood, D.J., and Werme, L. (2002). Anaerobic corrosion of carbon

519   steel and cast iron in artificial groundwaters: Part 1 – Gas generation. Corrosion,

520   58, 627-637.

521   Tripathy, S., Sriharan, A., and Schanz, T. (2004). Swelling pressure of compacted

522   bentonites from diffuse double layer theory. Canadian Geotechnical Journal, 41,

523   437-450.

524   Wang, X.K., Dong, W.M., Li, Z., Du, J.Z., and Tao Z.Y. (2000). Sorption and

525   desorption of radiocesium on red earth and its solid components: relative

526   contribution and hysteresis. Applied Radiation and Isotopes, 52, 813.

527   Wilson, J., Savage, D., Cuadros, J., Shibata, M., and Ragnarsdottir, K.V. (2006a). The

528   effect of iron on montmorillonite stability. (I). Background and thermodynamic

529   considerations. Geochimica et Cosmochimica Acta, 70, 306-322.

530   Wilson, J., Cressey, G., Cressey, B., Cuadros, J., Ragnarsdottir, K.V., Savage, D., and

531   Shibata M. (2006b). The effect of iron on montmorillonite stability. (II).

532   Experimental investigation. Geochimica et Cosmochimica Acta, 70, 323-336.

533

Revision 2

534

TABLE 1. Chemical composition (w/w %) of the stainless steel AISI 316 L used in this work

Co	V	Si	S	P	Mn	Cr	Fe	Ni	Cu	Mo	Cl
0.14	0.11	0.38	0.03	0.04	1.74	16.53	68.29	10.57	0.29	1.87	0.01

535

536

537

TABLE 2. pH and redox potential (E_h) values of the initial aqueous solution and the solution after hydrothermal reaction at 300ºC for 4.5 days of FEBEX in contact with a 7.9×10^{-2} M solution of Sm^{3+} and ZrO^{2+}.

Solution	Sm^{3+}		ZrO^{2+}	
	pH	E_h (mV)	pH	E_h (mV)
Initial	4.20	439	1.38	554
Final	2.47	547	1.55	614

Revision 2

538   **FIGURE CAPTIONS**

539

540   **FIGURE 1.** XRD diffraction patterns of the FEBEX smectite: a) Untreated FEBEX. b)

541   After being treated hydrothermally at 300ºC for 4.5 days with a solution of 7.9×10^{-2} M

542   Sm^{3+}. q=quartz (PDF 04-006-1757), c=cristobalite (PDF 04-008-7824), h=$H_2Si_2O_5$

543   (PDF 00-050-0439), and, n=nacrite 2M2 (PDF 01-072-2206).

544

545   **FIGURE 2.** SEM micrograph of: a) the original FEBEX. b) General view of the treated

546   FEBEX at 300ºC for 4.5 days in contact with a solution of 7.9×10^{-2} M Sm^{3+}.c) Other

547   zone from b) where block morphology, marked with ①, are shown. EDX spectra of: d)

548   the original FEBEX; (e) EDX of lamellar particles shown in b) after hydrothermal

549   reaction at 300ºC for 4.5 days with a solution of 7.9×10^{-2} M Sm^{3+}. f) EDX of block

550   morphology shown in fig. c)

551

552   **FIGURE 3.** XRD diffraction patterns of the minireactor after hydrothermal treatment at

553   300ºC in contact with a solution of 7.9×10^{-2} M Sm^{3+} for 4.5 days: a) without FEBEX b)

554   with FEBEX. c) After desorption process.

555

556   **FIGURE 4.** SEM Micrographs of the minireactor after hydrothermal reaction at 300ºC

557   for 4.5 days in contact with a solution of 7.9×10^{-2} M Sm^{3+}: a) General view. b-c) with

558   FEBEX. d-e) after desorption. EDX of different zones viewed in SEM micrographs: f)

559   EDX of the steel as-made. g) After hydrothermal reaction at 300ºC for 4.5 days in

560   contact with a solution of 7.9×10^{-2} M Sm^{3+}. h-i) in presence of FEBEX. j-k) After

561   desorption process.

562

Revision 2

563   **FIGURE 5.** a) SEM micrographs of a transverse section of the minireactor after

564   hydrothermal reaction at 300ºC for 4.5 days with FEBEX and a solution of $7.9x10^{-2}$ M

565   Sm^{3+}. b) Intensity profile of the elemental composition. c-d) after desorption process

566

567   **FIGURE 6.** XRD diffraction patterns of the FEBEX smectite: a) Untreated FEBEX. b)

568   After being treated hydrothermally at 300ºC for 4.5 days with a solution of $7.9x10^{-2}$ M

569   ZrO^{2+}. q=quartz (PDF 04-006-1757), and, c=cristobalite (PDF 04-008-7824).

570

571   **FIGURE 7.** SEM micrographs of the treated FEBEX at 300ºC for 4.5 days with a

572    $7.9x10^{-2}$ M solution of ZrO^{2+}: a) A general view; b) bright particles agglomerates

573   constituted mainly of zirconium; and; c) iron particles arising from container

574   degradation. EDX spectra of: d) lamellar particles shown in a) after hydrothermal

575   reaction at 300ºC for 4.5 days with a solution of $7.9x10^{-2}$ M of ZrO^{2+}; e) zirconium

576   agglomerates shown in b); f) EDX of iron particles shown in c); and; EDX spectrum of

577   FEBEX has been included as reference.

578

579   **FIGURE 8.** XRD diffraction patterns of the minireactor after hydrothermal treatment at

580   300 ºC in contact with a $7.9x10^{-2}$ M solution of ZrO^{2+} for 4.5 days: a) without FEBEX

581   b) with FEBEX. c) After desorption process.

582

583   **FIGURE 9.** SEM Micrographs of the minireactor after hydrothermal reaction at 300ºC

584   for 4.5 days in contact with a $7.9x10^{-2}$ M solution of ZrO^{2+}: a) General view. b-d) in

585   presence of FEBEX. e-f) after desorption process. g-l) The corresponding EDX spectra.

586

Revision 2

587 **FIGURE 10.** a) SEM Micrographs of a transverse section of the minireactor after

588 hydrothermal reaction at 300ºC for 4.5 days with FEBEX and a solution of 7.9×10^{-2} M

589 ZrO^{2+}. b) Intensity profile of the elemental composition. c-d) after desorption process.

590

591 **FIGURE 11.** pH-Redox potential (Eh) plot (Pourbaix diagrams) of the initial solution

592 (circle) and the supernatant recovered after hydrothermal treatment(triangle) for :a)

593 7.9×10^{-2} M Sm^{3+} , b) 7.9×10^{-2} M ZrO^{2+}.

594

Revision 2

595   *Fig. 1*

596
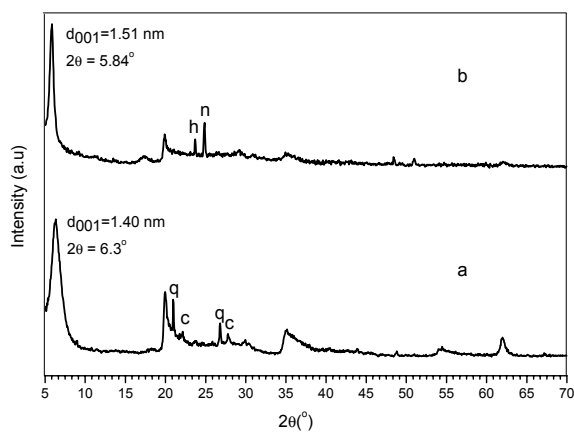
Revision 2

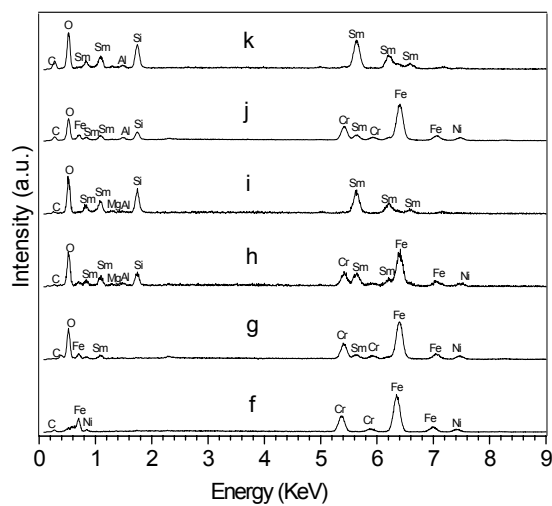597   Fig. 2
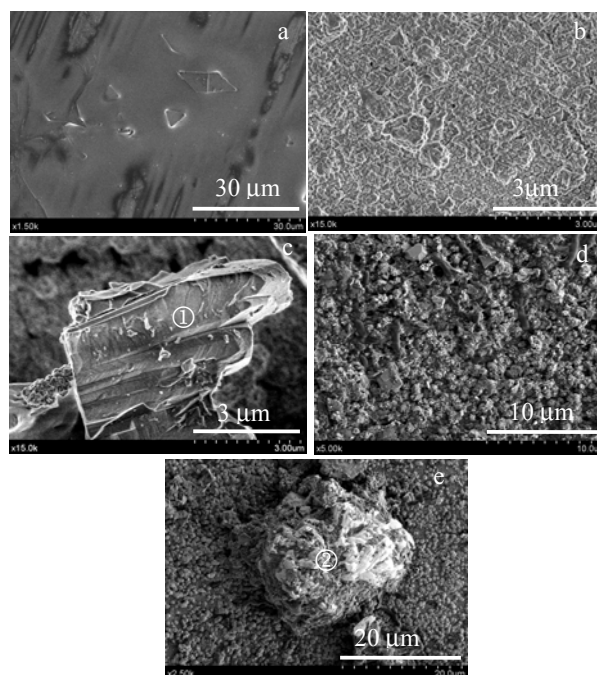
598

599
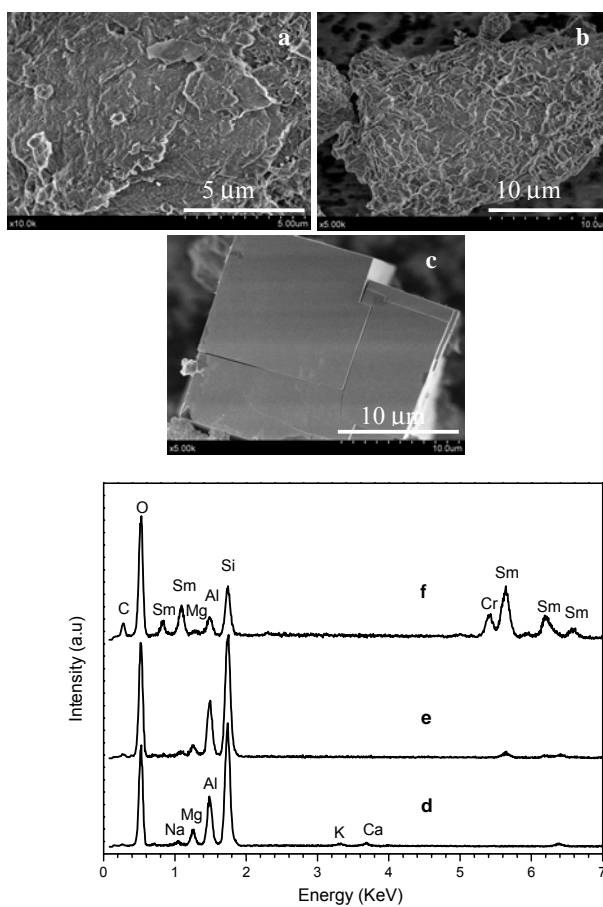
Revision 2

600   Fig. 3
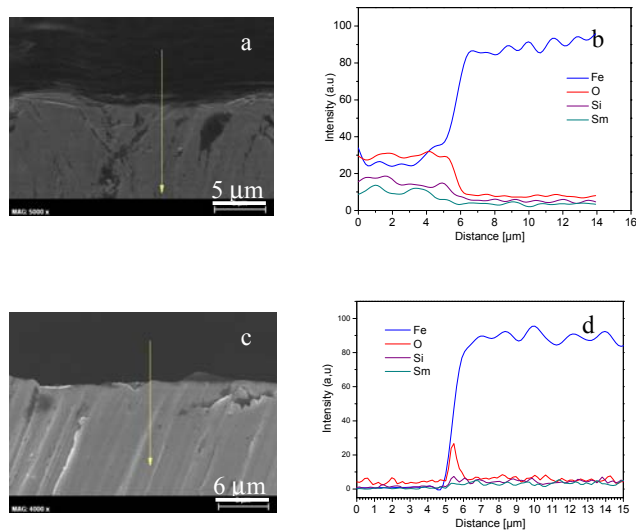
601

602
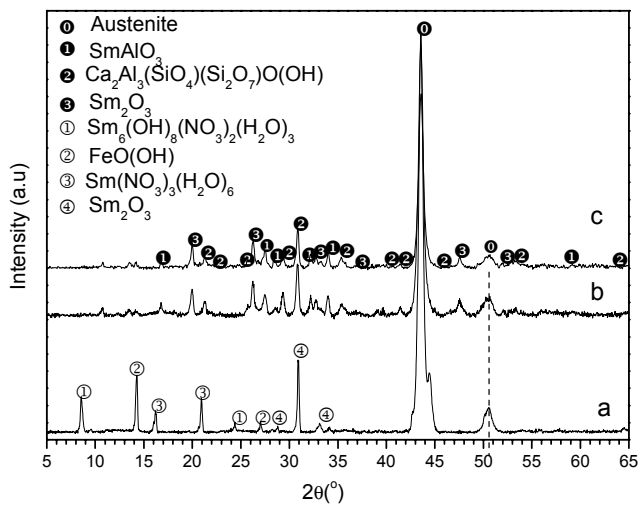
Revision 2

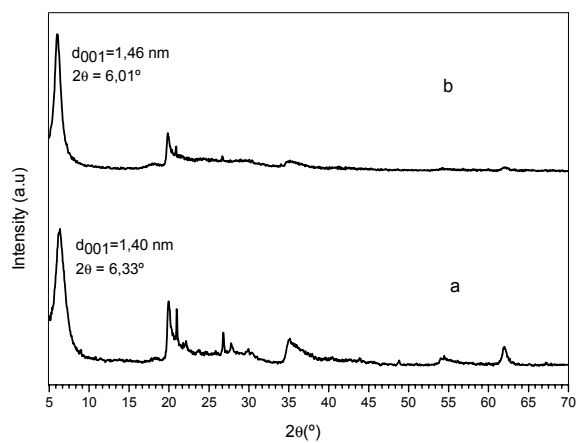603   Fig.4

604

605

Revision 2

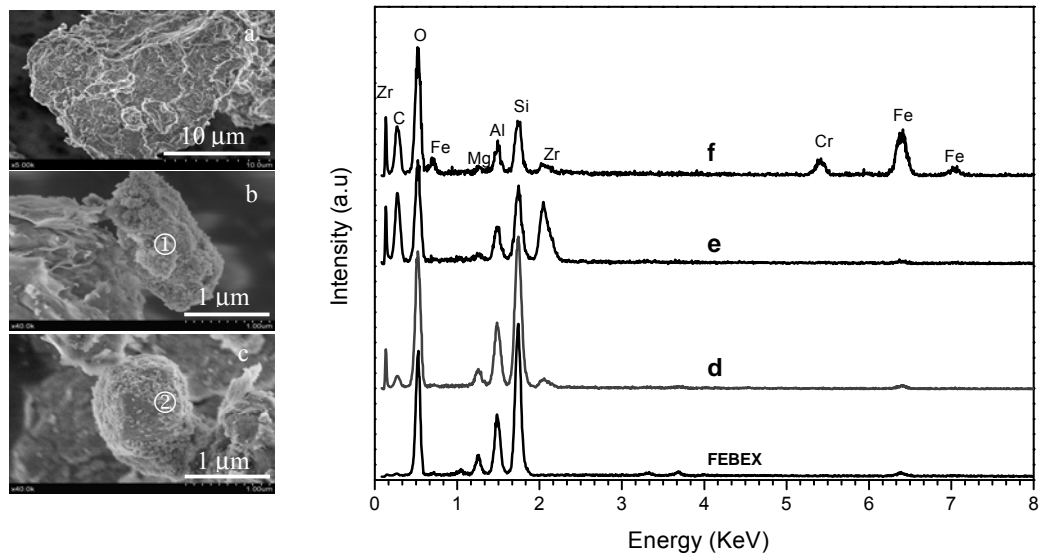606   Fig. 5

607

Revision 2

608   Fig. 6

609

610

Revision 2

611   Fig. 7

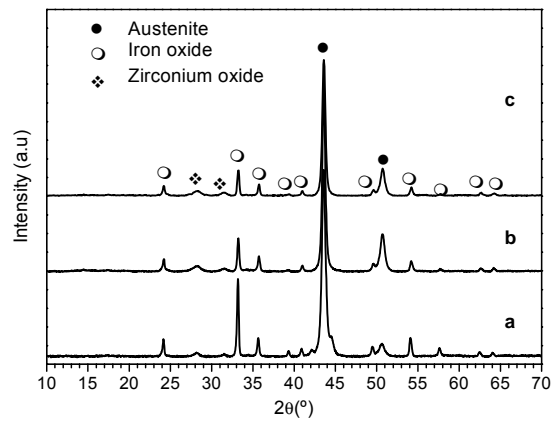Revision 2

612

Fig. 8

613

Revision 2

614   Fig. 9
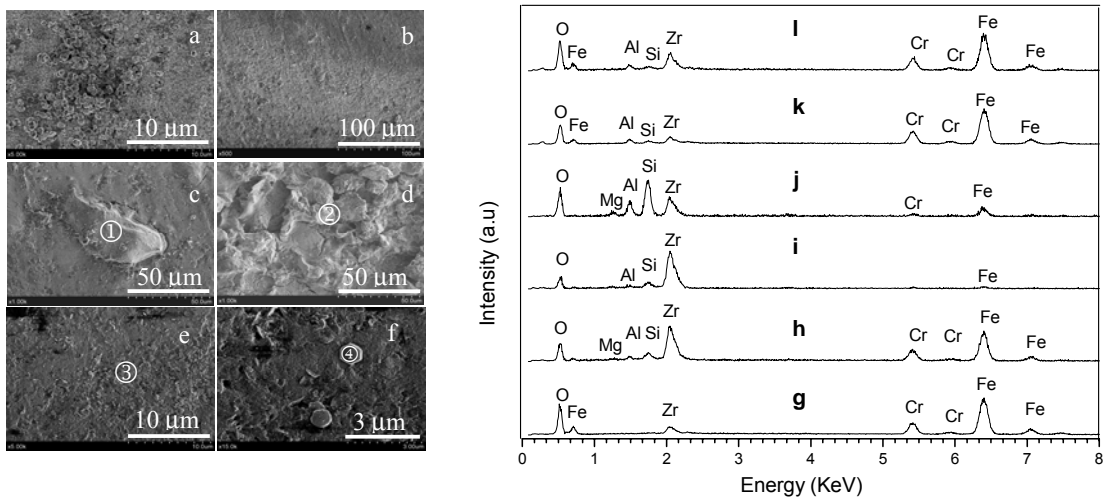
615

616

Revision 2

617   Fig. 10

618